

1

2 **Future global population exposure to record-breaking climate**

3 **extremes**

4 **Bohao Li^{1,2}, Kai Liu^{1,3,*}, Ming Wang¹, Qianzhi Wang^{1,4}, Qian He², Chenxia Li⁵**

5 ¹ School of National Safety and Emergency Management, Beijing Normal University, Beijing
6 100875, China.

7 ² Faculty of Geographical Science, Beijing Normal University, Beijing 100875, China.

8 ³ Collaborative Innovation Centre on Forecast and Evaluation of Meteorological Disasters (CIC-
9 FEMD), Nanjing University of Information Science & Technology, Nanjing 210044, China

10 ⁴ School of Systems Science, Beijing Normal University, Beijing 100875, China.

11 ⁵ College of Resources, Environment and Tourism, Capital Normal University, Beijing 100048,
12 China

13 *Corresponding author: Kai Liu (liukai@bnu.edu.cn)

14 **Key Points:**

- 15 • Africa and South America will experience successive record-breaking extreme events and
16 even compound drought and heatwaves.
- 17 • Population exposure is highly uneven and largely concentrated in underdeveloped areas.
- 18 • Record-breaking probability growth is the major driver of population exposure growth in
19 most regions of the world.

20 Abstract

21 The increase in record-breaking extreme events caused by climate change poses a threat to
22 human health and well-being; understanding the future impacts of such events on global
23 populations can provide decision-making support for policies aiming to mitigate climate change.
24 Here, we investigated the population exposure to eight climate extreme indices and drivers of
25 exposure trajectories based on NASA Earth Exchange Global Daily Downscaled Projections
26 Coupled Model Intercomparison Project 6 (CMIP6) and population projection data under four
27 shared socioeconomic pathway (SSP) scenarios at a spatial resolution of $0.25^\circ \times 0.25^\circ$. The results
28 show that by the mid-21st century, most regions around the world, especially Africa and South
29 America, will continue to experience record-breaking temperatures and compound drought and
30 heatwaves (CDHWs). Regarding population exposure, under the worst-case scenario of SSP3-
31 7.0 in the late 21st century, the mean value of the multimodel median expected annual exposure
32 (EAE) of all extreme temperature indices and CDHW reaches 8.79 billion persons per year;
33 population exposure hotspots will be concentrated in Central Africa, South Asia, Southeast Asia,
34 and East Asia, mostly in developing countries, where 62.77%-87.42% of the EAE is found. The
35 drivers of exposure trajectories are spatially heterogeneous; the increase in record-breaking
36 probability contributes more than population growth to EAE growth in most regions of the world
37 except Central Asia, the Middle East, and most of Africa. These findings highlight the necessity
38 of using various climate extreme indices to reveal spatiotemporal patterns of population exposure,
39 which can provide references for future adaptation decisions and risk management.

40 Plain Language Summary

41 Climate change causes unimaginable increases in extreme weather events that threaten human
42 health and well-being; understanding the future impacts of climate change on global population
43 can inform policies aiming to mitigate climate change. Here, we investigated the spatiotemporal
44 dynamics of future record-breaking extreme temperature and precipitation events, sequential
45 floods and heatwaves (hot extremes after flooding), and compound drought and heatwaves (co-
46 occurring dry and hot extremes) (CDHWs) and analyzed how populations may be potentially
47 affected by these events based on the latest available climate model data and future population
48 projections. The results show that by the mid-21st century, most regions around the world,
49 especially Africa and South America, will continue to experience record-breaking temperatures
50 and CDHWs. Regions where populations will be most affected include Central Africa, South

51 Asia, Southeast Asia, and East Asia, mostly developing countries. This increase in the affected
52 population is due to the growth of population and the increase of record-breaking extreme events;
53 record-breaking extreme event increase contributes more than population growth in most regions
54 of the world except Central Asia, the Middle East, and most of Africa. These findings confirm
55 the urgent need for adaptive measures and risk management to address future unprecedented
56 climate extremes.

57 **1 Introduction**

58 Increased frequency and intensity of climate extreme events such as droughts, heatwaves,
59 exceptional rainfall or floods caused by climate change have led to heightened human morbidity
60 and mortality and adverse impacts on mental health (Ebi et al., 2021; Grant, 2017). Moreover,
61 climate extreme events have downstream effects that harm human health and well-being by
62 affecting environmental systems, such as increasing the suitability of infectious disease
63 transmission and reducing the yield potentials of major crops (McMichael, 2015; Watts et al.,
64 2021). These implications are usually unequal, with disproportionate impacts on vulnerable
65 populations who contribute the least to the issue, which exacerbates social inequalities (Islam &
66 Winkel, 2017). In extreme event risk management, there is a tendency to adapt most to the
67 highest anomalies in the observed or historical archives, so that record-shattering extreme events
68 often result in significant damage (Fischer et al., 2021); for example, the unprecedented flood
69 that occurred in Zhengzhou, China, in 2021 disrupted the livelihoods of 3.98 million people and
70 killed 16 (Guo et al., 2023), the record-breaking heatwave that occurred in the UK in 2022 killed
71 3,200 people (Yule et al., 2023), and very extreme climate anomalies that occurred in Europe in
72 2003 led to persistent droughts and heatwaves resulting in at least 35,000 deaths (Ciais et al.,
73 2005). Exposure is the primary driver of risk and can reflect the situation of people in hazard-
74 prone areas (Kreibich et al., 2022). Accordingly, to ensure adaptive decision-making and risk
75 management, we must investigate the spatiotemporal pattern of future population exposure to
76 record-breaking extreme events to reveal the potential dangers of future extremes.

77 The above understanding is exceedingly critical and urgent for districts with high urbanization
78 rates and dense populations. Inspired by this concern, several studies have analyzed the spatial
79 and temporal patterns of population exposure to extreme temperature or precipitation under
80 different scenarios based on general circulation model (GCM) simulations (mainly Coupled

81 Model Intercomparison Project Phase 6 (CMIP6) data) at the global scale (H. Chen & Sun, 2021;
82 Klein & Anderegg, 2021; Park & Jeong, 2022) or identified hotspots of population exposure to
83 climate extremes such as South Asia (Kumar & Mishra, 2020; Zhao et al., 2021), East Asia (W.
84 Zhang & Zhou, 2020), North America (Bryan Jones et al., 2015; Swain et al., 2020), and Africa
85 (Fotso-Nguemo et al., 2023; Iyakaremye et al., 2021). Considering that isolated studies of
86 individual hazards performed through climate risk assessment may underestimate the amplifying
87 effects of multiple extreme event combinations, some studies have been conducted to explore the
88 population exposure to compound events (Das et al., 2022; Wang et al., 2020; G. Zhang et al.,
89 2022). These studies have typically estimated population exposure based on the predicted
90 frequency of future extreme events; however, extreme events have significantly broken long-
91 standing records in recent years, and the occurrence likelihood of record-shattering extremes has
92 increased, making it essential to reveal global population exposure to record-breaking extreme
93 events to assist policymakers in effectively reducing the risk caused by “Black Swan” events
94 (Fischer et al., 2021; Nangombe et al., 2018). Additionally, the spatial resolution of most studies
95 at the global scale is coarser than 1°, and such resolution cannot accurately capture the
96 population exposure variations within different regions; in addition, the use of different climate
97 extreme indices and GCMs makes it difficult to compare population exposure across extreme
98 events. Population exposure projections obtained for various extreme events at high spatial
99 resolution are crucial for facilitating cost-effective investments in adaptation measures and for
100 helping identifying which hazards different regions should prioritize adapting to.

101 To help decision-makers understand the potential threat to humanity from future global record-
102 breaking extreme events and develop accurate disaster-prevention and disaster-mitigation
103 measures in response to climate change and demographic variations, here, we use the National
104 Aeronautics and Space Administration (NASA) Earth Exchange Global Daily Downscaled
105 Projections CMIP6 (NEX-GDDP-CMIP6) data in combination with future population projection
106 data to analyze the global population exposure to multiple hazards under different future
107 scenarios at a relatively fine spatial resolution ($0.25^\circ \times 0.25^\circ$). The objectives of this study are
108 specified as follows: (1) to quantify hazards using climate extreme indices and demonstrate the
109 spatiotemporal dynamics of global future record-breaking probabilities for different indices
110 under each scenario; (2) to compare global future population exposures to different climate
111 extreme indices in different decades of the 21st century under each scenario globally and reveal

112 hotspots of population exposure in the late 21st century; and (3) to investigate population
 113 exposure trajectories and quantify how record-breaking probability and future population drive
 114 exposure trajectories in different regions.

115 **2 Materials and Methods**

116 **2.1 NEX-GDDP-CMIP6**

117 The NEX-GDDP-CMIP6 dataset provides global downscaled climate scenarios derived from
 118 CMIP6 GCM simulations at a spatial resolution of $0.25^\circ \times 0.25^\circ$ (approximately 25 km) generated
 119 based on the bias-correction spatial disaggregation method (Wood et al., 2004). This dataset
 120 consists of 35 GCMs at the daily scale, including simulations of the historical period (1950-
 121 2014) and four scenario composites that represent combined Shared Socioeconomic Pathway
 122 (SSP) and Representative Concentration Pathway (RCP) scenarios (SSP1-2.6, SSP2-4.5, SSP3-
 123 7.0, and SSP 5-8.5) for the future (2015-2100) (O'Neill et al., 2016). Most GCMs produce data
 124 that include nine meteorological variables (Thrasher et al., 2022). In this study, we used 22
 125 GCMs, all of which contained four SSP scenarios and key meteorological variables, including
 126 the near-surface relative humidity (hurs), precipitation (pr), daily near-surface air temperature
 127 (tas), daily maximum near-surface air temperature (tasmax), and daily minimum near-surface air
 128 temperature (tasmin) (Table S1); the SSP3-7.0 results were highlighted for analysis in this study,
 129 and the multimodel median was used for the spatiotemporal characterization. Table 1 provides
 130 brief descriptions of the scenarios used in this study.

131 **Table 1.** Description of climate scenarios considered in this study.

Scenario name	Forcing category	Global warming by 2100 compared to the preindustrial level	Description
SSP1-2.6	Low	1.8 °C	This pathway uses sustainable development policies and represents the low end of the future forcing pathways
SSP2-4.5	Medium	2.7 °C	SSP2-4.5 envisages an intermediate path in which the historical development pattern is continued
SSP3-7.0	High	3.6 °C	This pathway represents increased social inequality, rapid population growth, low investments in education and health, and relatively high forcing

SSP5-8.5	High	4.4 °C	This pathway assumes a fossil-based, energy-intensive economic development pattern, representing a very high emission scenario
----------	------	--------	--

132

133 2.2 Gridded population data

134 Jones & O'Neill (2016) produced grid cell-level population projections for five SSPs, SSP1,
135 SSP2, SSP3, SSP4, and SSP5, from 2010 to 2100 at a 10-year interval using the parameterized
136 gravity-based downscaling model; the data had a spatial resolution of $0.125^\circ \times 0.125^\circ$. In this
137 study, we used population projection data for the 2020-2100 under the four SSPs in Table 1 and
138 resampled the data to $0.25^\circ \times 0.25^\circ$ using a weighted summation method to match the NEX-
139 GDDP-CMIP6 data. Figure S1 shows the population trends from 2020 to 2090.

140 2.3 Climate reference regions

141 To better illuminate the spatiotemporal patterns of regional record-breaking probability and
142 population exposure for better understanding by citizens and scientists, we analyzed the key
143 results at a subcontinental scale based on climate reference regions (Figure S2) that take into
144 account precipitation and temperature distribution characteristics, as used by the
145 Intergovernmental Panel on Climate Change (IPCC) Sixth Assessment Report (AR6) (Iturbide et
146 al., 2020).

147 2.4 Climate extreme indices

148 We selected eight climate extreme indices that are relevant to human health and livelihoods
149 (Table 2). Three extreme precipitation indices, including the total precipitation (PRCPTOT),
150 maximum 1-day precipitation (RX1D), and number of days with heavy precipitation (R50), were
151 used to reflect the frequency and intensity of global precipitation. Three extreme temperature
152 indices, including warm days (Tx90p), warm nights (Tn90p), and heatwaves (HW), were
153 considered to analyze the effect of diurnal and consecutive heat extremes on public health. We
154 considered two types of compound events: sequential flood-heatwave (SFH) and compound
155 drought and heatwave (CDHW). The selection of these two compound indices was based on the
156 following concerns: extreme flooding may be closely associated with extreme heat, and the
157 electricity supply outages caused by floods make post-flood humid-heat events more likely to
158 trigger heat stress (Gu et al., 2022); and drought triggers wildfires that cause air pollution and

159 damage crops, thereby increasing the number of heatwave-related fatalities (Zscheischler et al.,
 160 2018). Here, the weighted average of precipitation (WAP) (Lu, 2009) is intended as a proxy for
 161 pluvial floods and is calculated as shown in Eq. 1:

$$WAP = (1 - a) \sum_{n=0}^N a^n P_n \quad (1)$$

162 where the parameter $a = 0.9$; we calculate the index in years, with N representing the number of
 163 days counting backward to the beginning of a year, n is the nth day of the year, and P_n is the
 164 daily precipitation on the nth day of the year. After a flood, the relatively high humidity may
 165 exacerbate human discomfort resulting from the effects of extreme heat, so we use the heat index
 166 (HI) (Anderson et al., 2013) instead of the daily maximum temperature to account for the SFH;
 167 the HI calculation formula is adopted from the National Weather Service (NWS) (NWS, 2011),
 168 and $HI > 40.6^\circ\text{C}$ is classified as extreme heat taking into account humidity in this study (Lin,
 169 2019). According to Chen et al. (2021), an SFH is defined as a consecutive occurrence of floods
 170 and heatwaves within a week. Drought events are identified using the standardized precipitation
 171 evapotranspiration index (SPEI) (Vicente-Serrano et al., 2010) on a 3-month time scale; CDHWs
 172 are considered as the frequency of heatwaves occurring during drought months ($SPEI < -1$) (Yin
 173 et al., 2023; Q. Zhang et al., 2022). Based on the python climate-indices library, we calculate the
 174 monthly potential evapotranspiration (PET) using the Thornthwaite method (Thornthwaite,
 175 1948) and the monthly near-surface air temperature data; then, we input the monthly PET and
 176 precipitation data to calculate SPEI. All indices are counted as annual time series. Table 2 shows
 177 the definitions of the climate extreme indices used in this study.

178 **Table 2.** The climate extreme indices chosen for this study

Category	Label	Index name	Definition	Unit
Extreme precipitation	PRCPTOT	Total precipitation	Annual total precipitation	mm
	RX1D	Maximum 1-day precipitation	Annual maximum 1-day precipitation	mm
	R50	Number of days with heavy precipitation	Number of days with daily precipitation $> 50 \text{ mm}$ in a year	days
Extreme temperature	Tx90p	Warm days	Number of days with maximum temperature $> 90\text{th}$ percentile of the	days

			historical period in a year	
Tn90p	Warm nights		Number of days with minimum temperature >90th percentile of the historical period in a year	days
HW	Heatwave		Number of times in a year when the maximum temperature >90th percentile of the historical period for more than 3 consecutive days	times
Compound events	SFH	Sequential flood-heatwave	Number of successive occurrences of floods (WAP >95th percentile of the historical period) and heatwaves (HI >40.6 °C for more than 3 consecutive days) within a week in a year	times
	CDHW	Compound drought and heatwave	Number of heatwaves (maximum temperature >90th percentile of the historical period) coinciding with monthly drought events (SPEI <-1) in a year	times

179

180 2.5 Record-breaking probability

181 For each annual time series of extreme climate indices, a record-breaking year is defined as a
 182 year in which the maximum value recorded during the historical period is exceeded; the annual
 183 record-breaking probability is calculated as the proportion of the record-breaking years in a
 184 given future period. We derived record-breaking probabilities on a grid scale for the late-21st
 185 century (2071-2100) and at decadal intervals from the 2020s to 2090s (for example, 2015-2024
 186 for the 2020s and 2085-2094 for the 2090s).

187 2.6 Population exposure

188 2.6.1 Exposure definitions

189 In this study, the annual population exposure refers to the population in a record-breaking year;
 190 combining record-breaking probabilities and population data, we use the expected annual
 191 exposure (EAE) to reveal the spatiotemporal distribution and dynamics of population exposure in
 192 persons per year, as obtained from Eq. 2:

$$EAE_T = Prob_T \times \frac{\sum_{n=0}^N Pop_n}{N} \#(2)$$

193 where T is the future period, $Prob$ is the record-breaking probability, Pop_n is the nth available
 194 population data in T , and N represents the number of available population data in T . Matching
 195 the record-breaking probabilities, gridded population exposures are generated for the late-21st
 196 century and the 2020s to 2090s at decadal intervals.

197 2.6.2 Exposure contributions

198 To investigate the importance of the population and record-breaking probability in the exposure
 199 trajectory, we quantified the shares of the population and record-breaking probability from the
 200 2020s to 2090s in EAE using Eq. 3 and Eq. 4 as follows:

$$EAE_{T,prob} = Prob_T \times Pop_{2020} \#(3)$$

$$EAE_{T,pop} = Prob_T \times \left(\frac{\sum_{n=0}^N Pop_n}{N} - Pop_{2020} \right) \#(4)$$

201 where $EAE_{T,prob}$ and $EAE_{T,pop}$ are the share of the record-breaking probability and the
 202 population to EAE_T , respectively, and Pop_{2020} refers to the population in 2020.

203

204 2.6.3 Exposure trends

205 Simple ordinary least squares (OLS) linear regression models were considered in this study to
 206 estimate the population exposure trends; to obtain the rate of change in exposure, we only
 207 retained areas with statistically significant increases ($p < 0.05$). We estimated the population
 208 exposure trends in persons per decade from the 2020s to 2090s and calculate the contributions of
 209 population increase and record-breaking probability increase to the variation in population
 210 exposure.

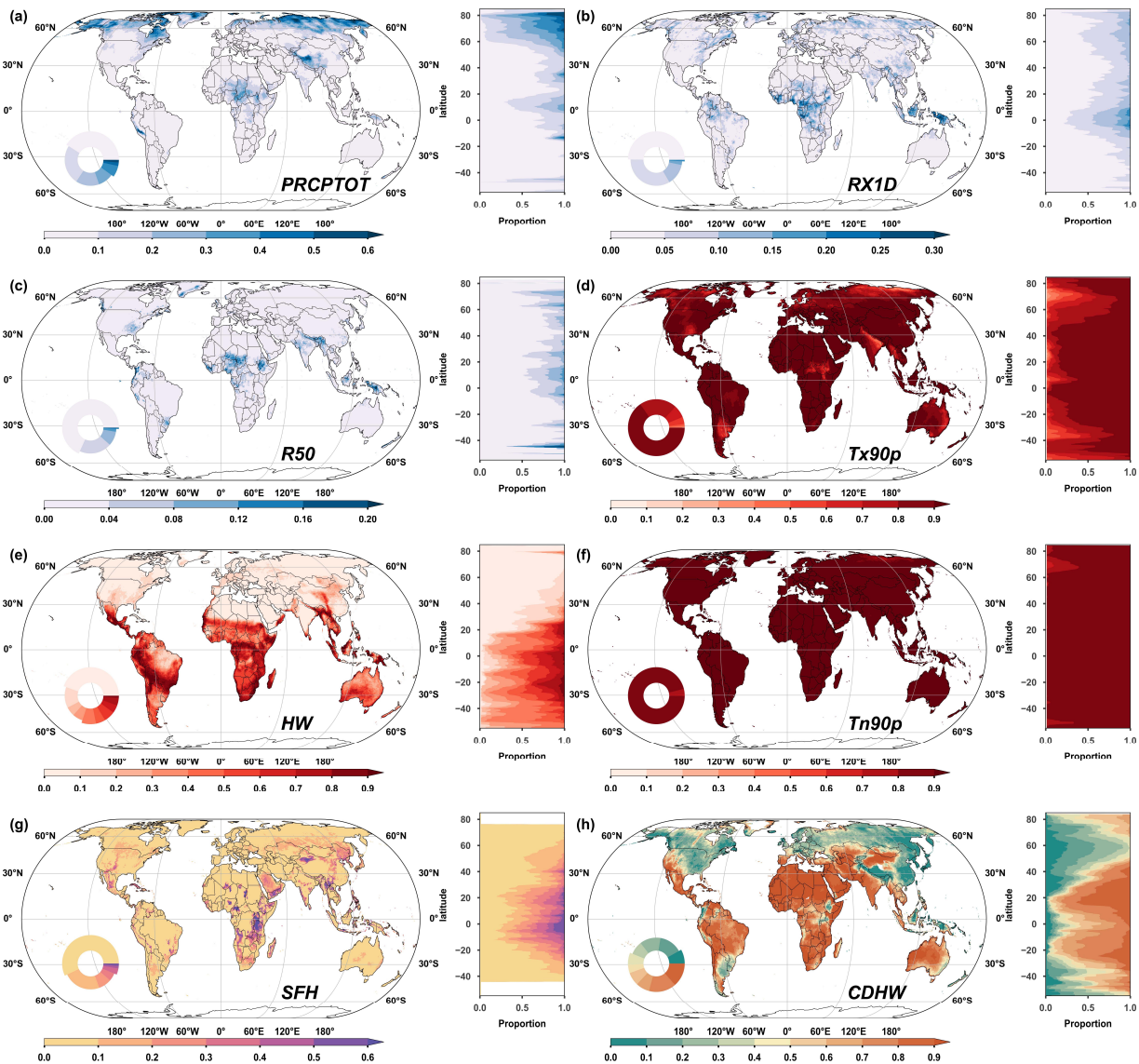
211

212 3 Results

213 3.1 Spatial and temporal patterns of global record-breaking probabilities

214 By the late-21st century, the spatial distribution patterns of record-breaking probabilities of
 215 extreme precipitation indices, HWs, and SFHs, are very similar under all four scenarios, while
 216 Tx90p, Tn90p, and CDHWs vary considerably across the four scenarios (Figure 1 and Figure S3-
 217 S5). Under the SSP3-7.0 scenario, the PRCPTOT record-breaking hotspots are concentrated on
 218 the Tibetan Plateau (TIB) and in the high-latitude regions of the Northern Hemisphere, including
 219 Alaska, Canada, the Arctic, and Northern Asia (NAS), with average record-breaking

probabilities of 13.4% and 16%, respectively (Figure 1a). The areas with the highest record-breaking probability of RX1D are mainly located in Central Africa (CAF) and Southeast Asia (SEA), both of which have 35% of the grid cells exceeding 10% probability (Figure 1b). In CAF and South Asia (SAS), where the R50 record-breaking probability is relatively high, only 9.6% and 10.6% of the grid cells' probability exceed 10%, respectively (Figure 1c). The record-breaking probabilities for Tx90p and Tn90p are extremely high, with global averages of 91.6% and 98.8%, meaning that almost the entire globe will be continuously affected by record-breaking extreme temperatures (Figure 1d and 1f). Most regions south of 30°N will experience a high record-breaking probability of HWs, especially in northern South America (NSA) and CAF, with averages of 39.1% and 34.6%, respectively (Figure 1e). The spatial variability in SFHs is high, with record-breaking probabilities exceeding 50% mainly in CAF, the TIB, SAS, and SEA, corresponding to 8.5%, 4.8%, 4.8%, and 4% of the grid cells, respectively; however, 68-81% of the grid cells in these regions have probabilities less than 10% (Figure 1g). CDHWs will have an overall high record-breaking probability south of 40°N, especially on the TIB and in Central America, Mexico, and the Caribbean (CAMC), Central Asia (CAS), SAS, and the Sahara (SAH), with average probabilities ranging from 52.5%-85.1%.



236
237 **Figure 1** Annual record-breaking probability projections of multimodel medians for different
238 climate extreme indices in the SSP3-7.0 scenario for the late-21st century: (a) PRCPTOT, (b)
239 RX1D, (c) R50, (d) Tx90p, (e) HW, (f) Tn90p, (g) SFH, and (h) CDHW. The rings show the
240 percentages of pixels corresponding to different record-breaking probability levels; the stacked
241 charts demonstrate the proportions of the record-breaking probability levels at different latitudes.

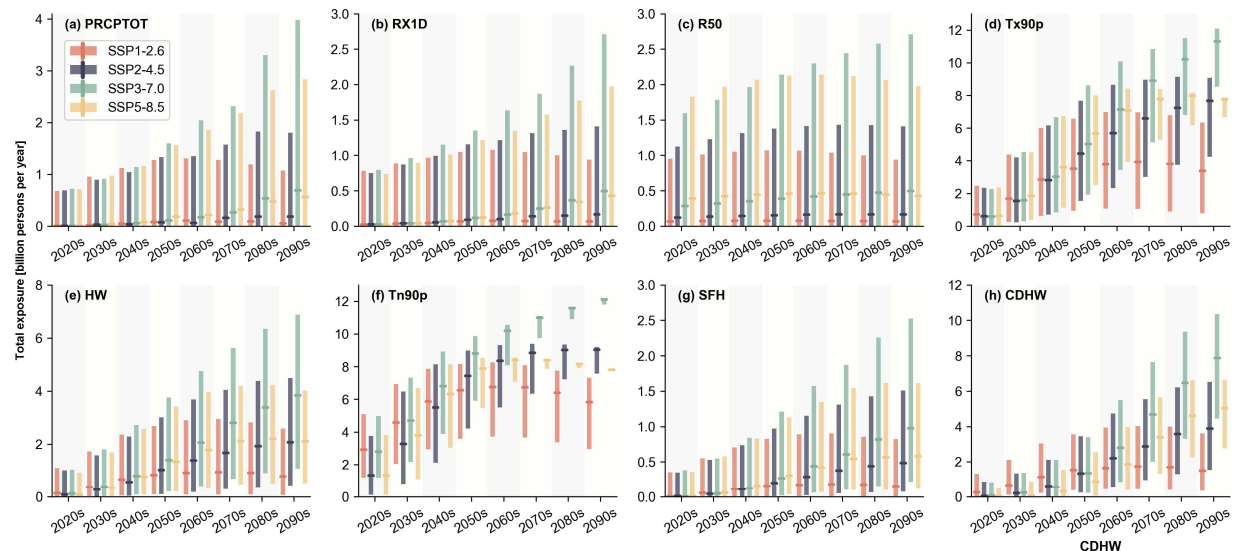
242 In dynamic terms, the record-breaking probabilities of all climate extreme indices show local or
243 nearly global increases from the 2020s to the 2090s under different scenarios, except the extreme
244 precipitation indices and SFHs, which do not change significantly under the SSP1-2.6 scenario
245 (Figure 2 and S6-S8). Figure S8 illustrates the record-breaking probability trends corresponding
246 to the indices under the SSP3-7.0 scenario. Record-breaking probabilities of extreme
247 precipitation will increase relatively slowly; the PRCPTOT growth rates exceed 5% per decade

248 in parts of the high-latitude Northern Hemisphere and on the TIB; RX1D and R50 both grow at
249 less than 5% per decade globally (Figure S8 a-c). The global average record-breaking probability
250 growth rates of Tx90p, Tn90p, and CDHW amount to 13.3%, 11.1%, and 8.3% per decade,
251 respectively; these results indicate that most regions of the world will be continuously exposed to
252 record-breaking heat events and even CDHWs by the middle of the 21st century (Figure S8d, f,
253 and h). The HW record-breaking growth hotspots are Australia and New Zealand (ANZ),
254 CAMC, CAF and Southern Africa (SAF), with average growth rates of 7.1%, 8.3%, 8.9%, and
255 10.1% per decade, respectively (Figure S8e). Although the global average SFH record-breaking
256 probability rate is not high, some regions will experience rapid growth (over 10% per decade),
257 primarily CAF and Asia (Figure S8g).

258 3.2 Global population exposure to climate extremes

259 Figure 2 depicts the total global multimodel EAE projections from the 2020s to 2090s. The
260 changes in EAE for extreme precipitation are very similar under different scenarios, with the
261 EAE increasing gradually with time for PRCPTOT and RX1D and remaining almost constant for
262 R50; under the two high-emission scenarios, the multimodel median EAE for PRCPTOT and
263 RX1D will reach 0.69 billion and 0.50 billion persons per year under the SSP3-7.0 scenario,
264 respectively, and 0.56 billion and 0.43 billion persons per year under the SSP5-8.5 scenario,
265 respectively, by the 2090s (Figure 2a-c). The EAE trends for extreme temperature and compound
266 events vary considerably across the four scenarios; under the SSP2-4.5 and SSP3-7.0 scenarios,
267 the global EAE of all indices except Tn90p continues to increase from the 2020s to the 2090s,
268 while under the SSP1-2.6 and SSP5-8.5 scenarios, the global EAE growth rate slows down after
269 the 2050s and even declines by the end of the 21st century (Figure 2d-h). Under the SSP3-7.0
270 scenario, the EAEs in the 2090s are very high for Tx90p, HW, Tn90p, and CDHW, with the
271 multimodel medians reaching 11.31 billion, 3.84 billion, 12.11 billion, and 7.88 billion persons
272 per year, respectively. The mean value of the multimodel medians of these four temperature
273 extreme indices reached 1.64-1.95 times the mean values of the multimodel medians of all
274 indices under different scenarios over time. The global population exposure to climate extremes
275 under the SSP3-7.0 scenario is more pronounced than that under other scenarios; this is
276 inextricably linked to the high population growth rates and emissions. Although the population
277 exposure to extreme precipitation is clearly lower than that to extreme temperature, the impacts

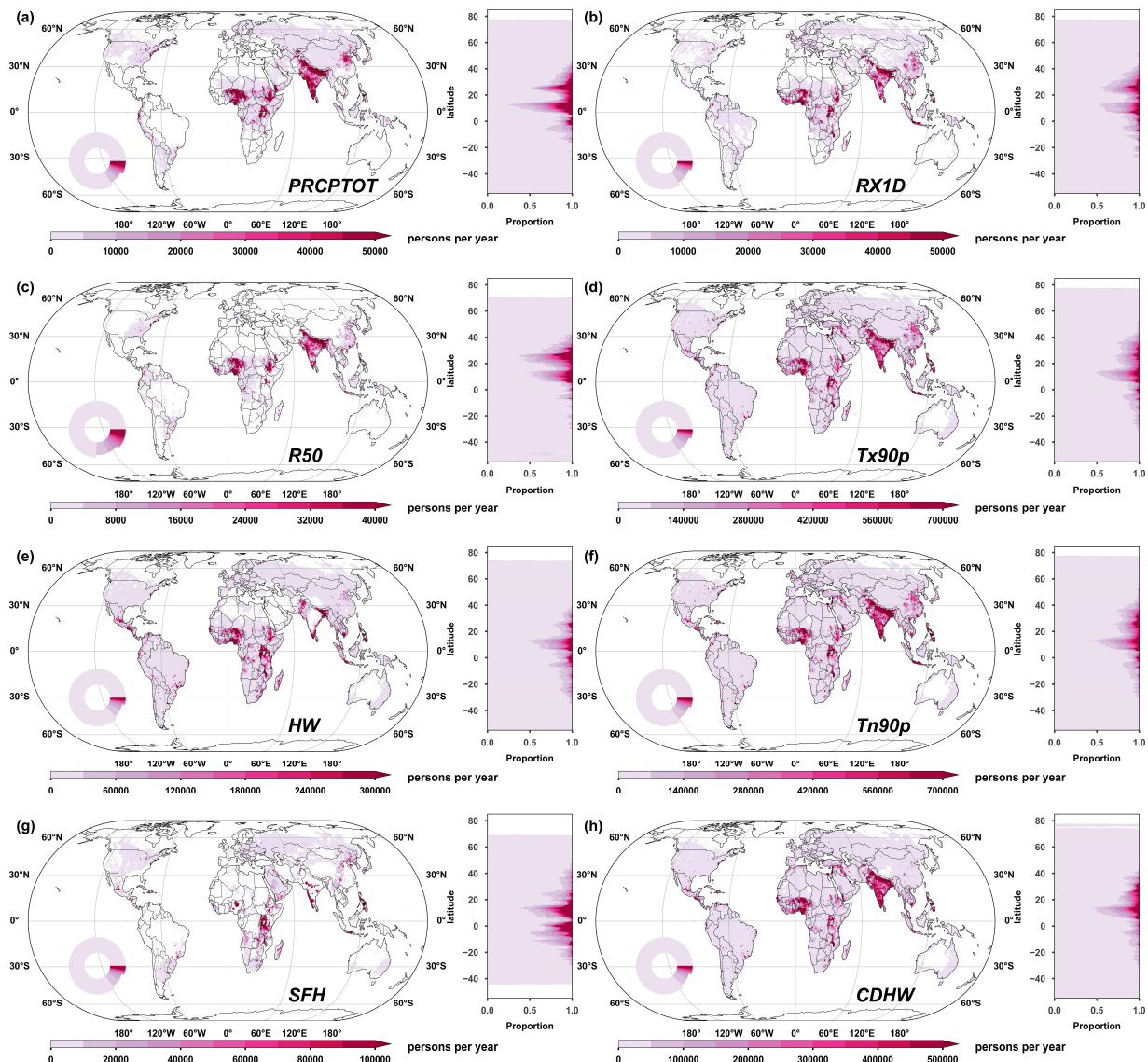
278 of extreme precipitation cannot be ignored, as extreme precipitation acts as a trigger for
 279 compound events that pose more serious hazards to humans, such as SFHs and CDHWs.



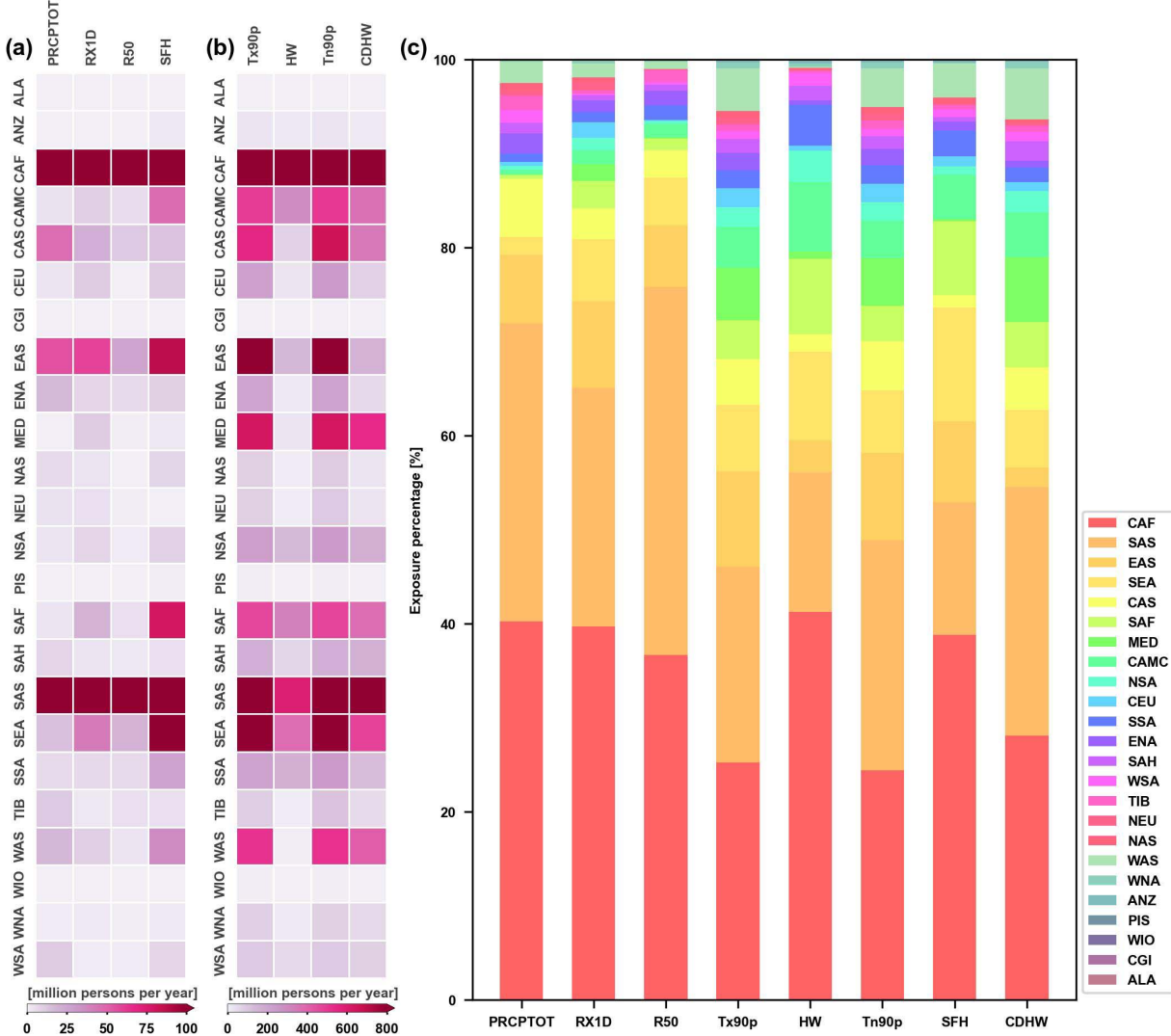
280
 281 **Figure 2** Total global EAE projections for different climate extreme indices under four scenarios
 282 from the 2020s to 2090s: (a) PRCPTOT, (b) RX1D, (c) R50, (d) Tx90p, (e) HW, (f) Tn90p, (g)
 283 SFH, and (h) CDHW. The range of bars refers to the multimodel 10th-90th percentiles of the
 284 EAE; the solid line in the middle is the multimodel median. The unit of total exposure is billion
 285 persons per year.

286 Figures 3 and 4 show the results of the global EAE projections for the late-21st century under the
 287 SSP3-7.0 scenario. Regions with high population exposure to all indices are concentrated in low
 288 and middle latitudes, mainly CAF, SAS, SEA, and East Asia (EAS); these areas contribute
 289 62.77%-87.42% to the EAE with 65.32% of the global population. Both CAF and SAS have very
 290 high EAEs for PRCPTOT, with the higher EAEs in CAF identified mainly in the western,
 291 eastern, and southeastern regions, while almost the whole region of India in SAS has high EAEs;
 292 13.47% and 37.8% of the grid cells in CAF and SAS, respectively, indicate exposures greater
 293 than 30,000 people per year (Figure 3a). The EAE hotspot areas for RX1D are similar to those
 294 for PRCPTOT, but RX1D has fewer high-EAE areas in CAF, SAS, and EAS (Figure 3b). The
 295 regions with high EAEs for R50 are clustered in CAF and SAS, with 6.97% and 21.75% of the
 296 grid cells in these regions having EAEs greater than 30,000 persons per year, respectively, while
 297 in other regions, such as the middle and high latitudes of the Northern Hemisphere, ANZ, and
 298 South America, the EAEs are very low (Figure 3c). Since Tx90p and Tn90p have very high
 299 record-breaking probabilities in the late-21st century, the global EAE to the two indices is almost
 300 identical to the global population distribution, with the EAEs of CAF, SAS, and EAS all

301 exceeding 800 million people per year (Figures 3d and f). The spatial distribution pattern of the
 302 EAE of CDHW is very similar to that of Tx90p; the only difference is that CDHWs have very
 303 low EAEs in the EAS (Figure 3h). The EAE hotspots for HW are primarily located in CAF, the
 304 border regions of India in SAS, and SEA, where 20.53%, 16.94%, and 10.03% of the grid cells
 305 have EAEs exceeding 100,000 people per year, respectively; although the EAEs of Tx90p are
 306 high in east-central China, the EAEs of HW are relatively low (Figure 3e). SFHs have high
 307 EAEs in CAF, SAS, SEA, and EAS, with 6.44%, 4.81%, 3.55%, and 0.70% of the grid cells
 308 having EAEs surpassing 100,000 people per year, respectively; notably, the population exposure
 309 of SFH in EAS is almost exclusively located along the Hu Huanyong Line in China (Figure 3g).



311 **Figure 3** EAE projections of multimodel medians for different climate extreme indices in the
 312 SSP3-7.0 scenario for the late-21st century: (a) PRCPTOT, (b) RX1D, (c) R50, (d) Tx90p, (e)
 313 HW, (f) Tn90p, (g) SFH, and (h) CDHW. The rings show the percentages of pixels
 314 corresponding to different population exposure levels; the stacked charts demonstrate the
 315 population exposure proportion at each level at different latitudes.



316 **Figure 4** Subcontinental EAE projections of the multimodel medians for different climate
 317 extreme indices in the SSP3-7.0 scenario for the late-21st century: (a) PRCPTOT, RX1D, R50,
 318 SFH, (b) Tx90p, HW, Tn90p, CDHW, and (c) regional percentages of the total global EAE.
 319 We calculated the EAEs under other scenarios in the late-21st century and derived essentially the
 320 same spatial population exposure pattern in the different scenarios (Figure S10-15). The global
 321 EAEs for all climate extreme indices under SSP3-7.0 are 2.35-8.32, 1.44-3.05, and 1.34-1.97
 322 times higher than those under SSP1-2.6, SSP2-4.5, and SSP5-8.5, respectively (Table S2). SAS
 323 has the largest EAE variation among all the subcontinental regions across all scenarios; under the
 324

325 SSP1-2.6 scenario, SAS has an evidently lower global share of EAE for most indices compared
326 to other scenarios.

327 3.3 Population exposure trends and exposure trajectory drivers

328 Figure S18 demonstrates the spatial distribution of the global EAE growth rates under the SSP3-
329 7.0 scenario, with hotspot areas similar to those of the EAE in the late-21st century. The EAEs of
330 certain indices exhibit relatively low growth rates in some regions, but high EAEs are still
331 expected by the late-21st century, which is the case for RX1D in northeast India, R50 in China
332 and India, and Tn90p in southern China. These regions have typically experienced high EAEs in
333 the 2020s, thus increasing the need for measures to combat weather extremes and protect
334 citizens. We analyzed the global EAE trends under the other scenarios and concluded that the
335 global EAE growth rates for different indices under the SSP3-7.0 scenario are 3.52-59.98, 1.21-
336 6.76, and 0.96-1.70 times higher than those under the SSP1-2.6, SSP2-4.5, and SSP5-8.5
337 scenarios, respectively (Table S3) (Figure S16-S19).

338 Figure 5 demonstrates a strong spatial divergence pattern in the shares of record-breaking
339 probability increase rates and population increase rates to EAE growth rates for all indices under
340 the SSP3-7.0 scenario. In CAS, the Middle East in West Asia (WAS), and the majority of Africa,
341 population growth contributes more than record-breaking probability growth; except these
342 regions, most of the global region is dominated by record-breaking probability growth driving
343 EAE growth. Under the SSP3-7.0 scenario, the contribution of record-breaking probability
344 growth rates to EAE growth rates under different indices ranges from 48.75% to 62.30%, and
345 this scenario predicts the lowest contribution of record-breaking probability growth rate to the
346 EAE growth rate. The shares of record-breaking probability growth rates under the SSP1-2.6,
347 SSP2-4.5, and SSP5-8.5 scenarios are 1.59-2.07, 1.27-1.51, and 1.50-1.83 times higher than that
348 under the SSP3-7.0 scenario, respectively (Table S4) (Figures S20-22).

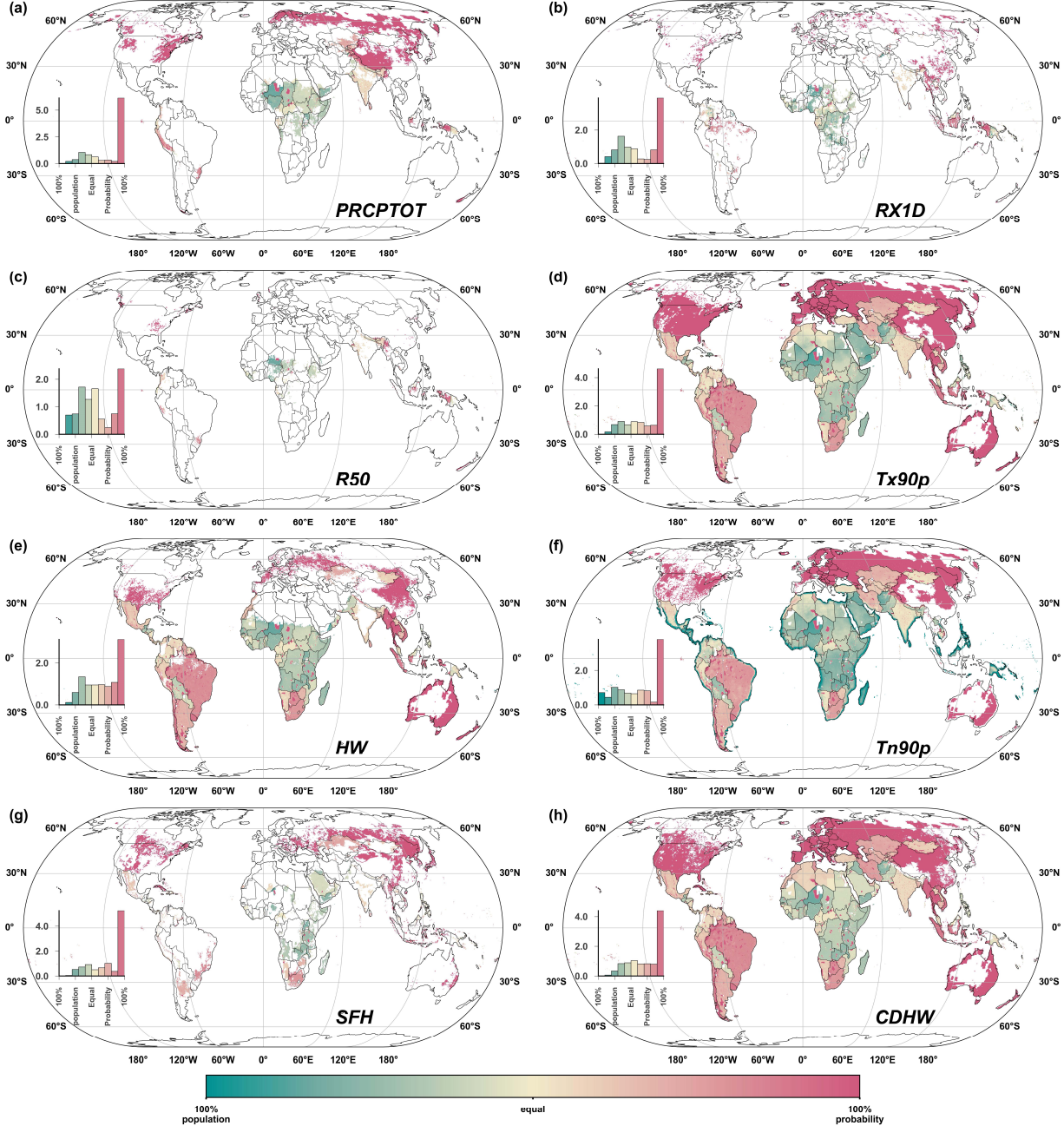
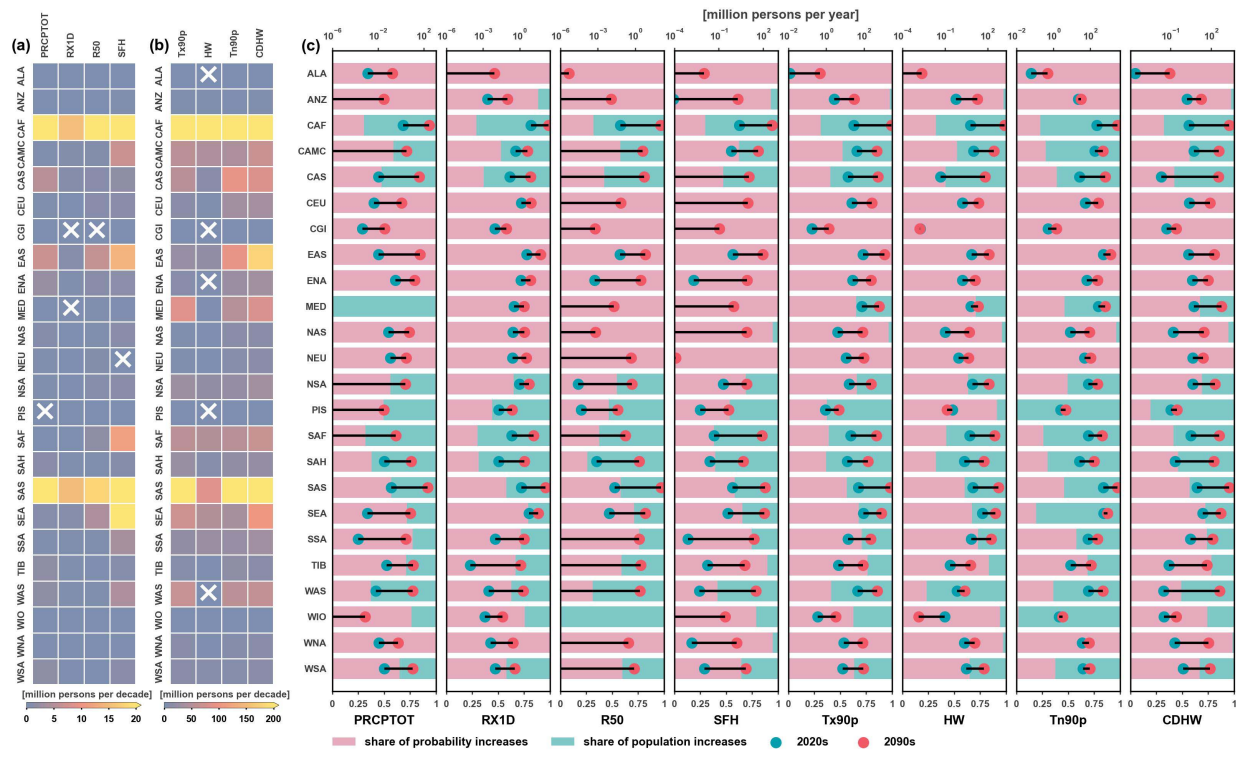


Figure 5 Contributions of record-breaking probability growth and population growth to the multimodel median EAE growth rates for different climate extreme indices projected under the SSP3-7.0 scenario: (a) PRCPTOT, (b) RX1D, (c) R50, (d) Tx90p, (e) HW, (f) Tn90p, (g) SFH, and (h) CDHW. The histograms depict the probability densities at different contribution levels.

Next, we detailed how the EAEs are expected to change from the 2020s to the 2090s in different regions of the globe at subcontinental scales and analyze how signals from demographics and record-breaking probabilities drive the exposure trajectories in each region (Figure 6 and Figures S23-25). Under the SSP3-7.0 scenario, the EAEs for different indices are predicted to increase

358 considerably in most regions of the world, with the EAEs in CAF and SAS for PRCPTOT,
 359 RX1D, R50, and SFH experiencing growth rates exceeding 10 million persons per decade, and
 360 for Tx90p, HW, Tn90p, and CDHW having EAE growth rates over 100 million persons per
 361 decade (Figure 6a and b). CAF and SAS, two regions with similar exposure trajectories, differ
 362 sharply in the importance of the demographic condition and record-breaking probabilities to the
 363 EAE growth rates; the share of record-breaking probability growth in CAF ranges from 67.52%
 364 to 76.93% for different climate extreme indices, while the share of record-breaking probability
 365 growth in SAS ranges from only 40.04% to 53.82% (Figure 6c). In addition, regions with
 366 negative or slight variations in the population growth rate (Figure S1 c), as represented by the
 367 EAS, have exposure trajectories driven entirely by record-breaking probabilities. Some indices
 368 have very high record-breaking probabilities as early as the 2020s and very low record-breaking
 369 probability increase rates, and thereby exposure trajectories are dominated by population
 370 changes; for example, Tn90p is prone to break records in coastal regions such as the West Indian
 371 Ocean (WIO) and Pacific Islands (PIS), where the share of population growth is 100%.
 372 Uncovering the spatially distinct patterns of exposure trajectory drivers is essential because such
 373 differences can effectively assist decision-makers in understanding the costs and benefits of local
 374 adaptations (Estrada et al., 2017; Tuholske et al., 2021).



376 **Figure 6** Subcontinental multimodel median EAE variations under the SSP3-7.0 scenario for
377 different climate extreme indices from the 2020s to 2090s: (a) EAE growth rates for PRCPTOT,
378 RX1D, R50, and SFH, (b) EAE growth rates for Tx90p, HW, Tn90p, and CDHW, and (c) shares
379 of the population growth and record-breaking probability growth contributing to the EAE
380 increase in the 2020s and 2090s. The “ \times ” symbols in panels (a) and (b) denote nonsignificant
381 EAE growth (p value <0.05).

382 To capture the drivers of exposure trajectories within typical regions at the subcontinental scale,
383 we selected the regions with the top three multimodel median EAE growth rates for each climate
384 extreme index under the SSP3-7.0 scenario to demonstrate the distribution of drivers of EAE
385 growth rates (Figure S26). The distributions of the exposure trajectories of the different climate
386 extreme indices are very similar within the same region, and for each index, the spatial
387 variability of exposure trajectories is high within the regions. CAF and SAS both have very high
388 population growth rates; the shares of these two drivers are similar in most of the SAS region,
389 and the share of the record-breaking probability increase is greater than that of the population
390 growth in a few SAS regions, while population growth rates dominate the exposure trajectories
391 in most of CAF. The increase in EAE within EAS will be caused almost entirely by increased
392 record-breaking probability due to negative population growth. In approximately half of the SEA
393 region, the two drivers have similar shares, while in the other half of the region, the exposure
394 trajectory is dominated by record-breaking probability. CDHWs have relatively high EAE
395 growth rates in South Europe and the Mediterranean (MED), where the exposure trajectory will
396 be almost entirely driven by record-breaking probability increases in about half of the MED
397 (mainly northern Europe), and the share of the two drivers will be similar in the other half
398 (mainly Northern Africa).

399 **4 Discussion and Conclusion**

400 In this study, we used NEX-GDDP-CMIP6 data to derive the record-breaking probabilities of
401 eight climate extreme indices from 22 GCMs under four scenarios; we then analyzed the
402 spatiotemporal dynamics of population exposure in conjunction with population projection data
403 and analyzed the drivers of the derived exposure trajectories. We found that the accelerated
404 development of relatively high emissions will significantly increase the global record-breaking
405 probabilities of extreme events. The record-breaking probabilities of extreme precipitation events
406 and SFHs are expected to increase at much lower rates than extreme temperature events and
407 CDHWs. Except for the SSP1-2.6 scenario, where almost no increase in the global record-

408 breaking probability of extreme precipitation events or SFHs is predicted, all climate extreme
409 indices show some increase in record-breaking probabilities in different regions of the world
410 under the different scenarios analyzed herein. The population exposure in the late 21st century is
411 expected to be very high under the SSP3-7.0 scenario, with the multimodel medians of different
412 indices being 2.35-8.32, 1.44-3.05, and 1.34-1.97 times higher than those obtained under the
413 SSP1-2.6, SSP2-4.5, and SSP5-8.5 scenarios, respectively. The population exposure to extreme
414 precipitation events and SFHs is much smaller than that to extreme temperature events and
415 CDHWs. In the late 21st century, most of the EAEs under all scenarios will be concentrated in
416 CAF, SAS, SEA, and EAS, except under the SSP5-8.5 scenario, where East North America
417 (ENA) will be another population exposure hotspot. Although the SSP5-8.5 scenario conferred
418 the highest record-breaking probabilities of extreme events, the population exposure under this
419 scenario is expected to be much lower than that under SSP3-7.0, reflecting the fact that
420 management policies regarding population development will significantly impact the future
421 population exposure. Understanding the drivers of future exposure trajectories is particularly
422 important for risk management. Here, we provide a detailed explanation of the spatial
423 heterogeneity corresponding to the ways in which population and record-breaking probability are
424 expected to drive global population exposure trajectories. In all four scenarios analyzed in this
425 study, the share of record-breaking probability increases to the global population exposure
426 growth is higher than the share of population growth, with only the SSP3-7.0 scenario predicting
427 a relatively high share of population growth. In CAS, the Middle East in WAS, and the majority
428 of Africa, the exposure trajectories will be predominantly population-driven, while in other
429 regions, the exposure trajectories will be mainly record-breaking probability-driven.

430 Although our study focuses on population exposure to record-breaking extreme events and our
431 results cannot be compared directly to previous work performed at the global or regional scales,
432 the population exposure hotspots identified in this study mostly correspond to areas with high
433 population exposure to extreme events, such as CAF, SAS, and EAS in previous studies. There
434 are certain limitations and potential improvements to this study. First, we ignored demographic
435 characteristics, such as age, gender, education, and income, which can indicate the vulnerability
436 of the population and influence the mortality rate of population affected by climate extremes; this
437 is a common problem faced in relevant studies, and few comparable historical datasets are
438 available to provide vulnerability information in large-scale studies (Coffel et al., 2017;

439 Iyakaremye et al., 2021; Weber et al., 2020). In addition, we used the extreme state of the WAP
440 to represent flooding, and this assumption lacks consideration of non-precipitation factors such
441 as land cover and flood management infrastructure. A combination of extreme indices and
442 hydrodynamic models may allow for better flood predictions (Y. Chen et al., 2021). We
443 concentrated only on extreme heat and extreme humid-heat events while ignoring other
444 meteorological features, such as wind speed and solar radiation that may impact humans. The use
445 of multiple location-based heat indices can forge good synergies for research domains such as
446 the global scale considered herein (Tuholske et al., 2021; Vanos et al., 2020). As socioeconomic
447 development increases the awareness of and preparedness for extreme events, there is a need to
448 dynamically consider the historical record of extreme events to accurately capture future record-
449 breaking probabilities. The definitions of the climate extreme indices and record-breaking
450 probabilities used in this study somewhat diminished the impacts of extreme event intensities.
451 Designing some metrics that quantify both the intensity and frequency of extreme events could
452 effectively solve this issue (Q. Zhang et al., 2022). Moreover, there is uncertainty in the
453 projection data used in this study. Gridded population projections ignore the potential impacts of
454 climate change, such as extreme drought-induced migration, which will be a priority issue in the
455 future (B. Jones & O'Neill, 2016). We used many GCMs to perform a comparative analysis of
456 multiple extreme events, but the predictions of future climate patterns varied considerably among
457 GCMs, especially the predictions of precipitation patterns. Applying optimal bias-correction
458 methods could reduce this uncertainty (Coffel et al., 2017; Levy et al., 2013).

459 The global population exposure to extreme events is highly unequal, with developing countries
460 in particular having much greater population exposures than developed countries. While we must
461 strive to keep the development pathway in accordance with the SSP1-2.6 scenario to prevent
462 serious impacts from climate change, addressing socioeconomic and infrastructure issues
463 through adaptation measures and financial assistance will be effective in reducing the damages
464 caused by climate change. For developing countries, it will certainly be a challenge to manage
465 risks with the limited funds available. The findings of this study could help drive future policy-
466 making related to climate change mitigation and controlling population growth to ensure a
467 sustainable future worldwide.

468 **Acknowledgements**

469 This work was supported by the National Natural Science Foundation of China (grant number
470 41771538). The financial support is highly appreciated.

471

472 **Open Research**

473 The data used in this study is available at <https://doi.org/10.6084/m9.figshare.22767122.v1>.

474 The NEX-GDDP CMIP6 dataset can be accessed at [https://www.nccs.nasa.gov/services/data-
475 collections/land-based-products/nex-gddp-cmip6](https://www.nccs.nasa.gov/services/data-collections/land-based-products/nex-gddp-cmip6).

476 **References**

- 477 Anderson, G. B., Bell, M. L., & Peng, R. D. (2013). Methods to Calculate the Heat Index as an
478 Exposure Metric in Environmental Health Research. *Environmental Health Perspectives*,
479 121(10), 1111–1119. <https://doi.org/10.1289/ehp.1206273>
- 480 Chen, H., & Sun, J. (2021). Significant Increase of the Global Population Exposure to Increased
481 Precipitation Extremes in the Future. *Earth's Future*, 9(9), e2020EF001941.
482 <https://doi.org/10.1029/2020EF001941>
- 483 Chen, Y., Liao, Z., Shi, Y., Tian, Y., & Zhai, P. (2021). Detectable Increases in Sequential
484 Flood-Heatwave Events Across China During 1961–2018. *Geophysical Research Letters*, 48(6),
485 e2021GL092549. <https://doi.org/10.1029/2021GL092549>
- 486 Ciais, P., Reichstein, M., Viovy, N., Granier, A., Ogée, J., Allard, V., et al. (2005). Europe-wide
487 reduction in primary productivity caused by the heat and drought in 2003. *Nature*, 437(7058),
488 529–533. <https://doi.org/10.1038/nature03972>
- 489 Coffel, E. D., Horton, R. M., & Sherbinin, A. de. (2017). Temperature and humidity based
490 projections of a rapid rise in global heat stress exposure during the 21st century. *Environmental
491 Research Letters*, 13(1), 014001. <https://doi.org/10.1088/1748-9326/aaa00e>
- 492 Das, J., Manikanta, V., & Umamahesh, N. V. (2022). Population exposure to compound extreme
493 events in India under different emission and population scenarios. *Science of The Total
494 Environment*, 806, 150424. <https://doi.org/10.1016/j.scitotenv.2021.150424>
- 495 Ebi, K. L., Vanos, J., Baldwin, J. W., Bell, J. E., Hondula, D. M., Errett, N. A., et al. (2021).
496 Extreme Weather and Climate Change: Population Health and Health System Implications.
497 *Annual Review of Public Health*, 42(1), 293–315. <https://doi.org/10.1146/annurev-publhealth-012420-105026>
- 499 Estrada, F., Botzen, W. J. W., & Tol, R. S. J. (2017). A global economic assessment of city
500 policies to reduce climate change impacts. *Nature Climate Change*, 7(6), 403–406.
501 <https://doi.org/10.1038/nclimate3301>
- 502 Fischer, E. M., Sippel, S., & Knutti, R. (2021). Increasing probability of record-shattering
503 climate extremes. *Nature Climate Change*, 11(8), 689–695. <https://doi.org/10.1038/s41558-021-01092-9>
- 505 Fotso-Nguemo, T. C., Weber, T., Diedhiou, A., Chouto, S., Vondou, D. A., Rechid, D., & Jacob,
506 D. (2023). Projected Impact of Increased Global Warming on Heat Stress and Exposed
507 Population Over Africa. *Earth's Future*, 11(1), e2022EF003268.
508 <https://doi.org/10.1029/2022EF003268>
- 509 Grant, P. R. (2017). Evolution, climate change, and extreme events. *Science*, 357(6350), 451–
510 452. <https://doi.org/10.1126/science.aoa2067>
- 511 Gu, L., Chen, J., Yin, J., Slater, L. J., Wang, H.-M., Guo, Q., et al. (2022). Global Increases in
512 Compound Flood-Hot Extreme Hazards Under Climate Warming. *Geophysical Research Letters*,
513 49(8), e2022GL097726. <https://doi.org/10.1029/2022GL097726>

- 514 Guo, X., Cheng, J., Yin, C., Li, Q., Chen, R., & Fang, J. (2023). The extraordinary Zhengzhou
515 flood of 7/20, 2021: How extreme weather and human response compounding to the disaster.
516 *Cities*, 134, 104168. <https://doi.org/10.1016/j.cities.2022.104168>
- 517 Islam, N., & Winkel, J. (2017). Climate change and social inequality.
- 518 Iturbide, M., Gutiérrez, J. M., Alves, L. M., Bedia, J., Cerezo-Mota, R., Cimadevilla, E., et al.
519 (2020). An update of IPCC climate reference regions for subcontinental analysis of climate
520 model data: definition and aggregated datasets. *Earth System Science Data*, 12(4), 2959–2970.
521 <https://doi.org/10.5194/essd-12-2959-2020>
- 522 Iyakaremye, V., Zeng, G., Yang, X., Zhang, G., Ullah, I., Gahigi, A., et al. (2021). Increased
523 high-temperature extremes and associated population exposure in Africa by the mid-21st
524 century. *Science of The Total Environment*, 790, 148162.
525 <https://doi.org/10.1016/j.scitotenv.2021.148162>
- 526 Jones, B., & O'Neill, B. C. (2016). Spatially explicit global population scenarios consistent with
527 the Shared Socioeconomic Pathways. *Environmental Research Letters*, 11(8), 084003.
528 <https://doi.org/10.1088/1748-9326/11/8/084003>
- 529 Jones, Bryan, O'Neill, B. C., McDaniel, L., McGinnis, S., Mearns, L. O., & Tebaldi, C. (2015).
530 Future population exposure to US heat extremes. *Nature Climate Change*, 5(7), 652–655.
531 <https://doi.org/10.1038/nclimate2631>
- 532 Klein, T., & Anderegg, W. R. L. (2021). A vast increase in heat exposure in the 21st century is
533 driven by global warming and urban population growth. *Sustainable Cities and Society*, 73,
534 103098. <https://doi.org/10.1016/j.scs.2021.103098>
- 535 Kreibich, H., Van Loon, A. F., Schröter, K., Ward, P. J., Mazzoleni, M., Sairam, N., et al.
536 (2022). The challenge of unprecedented floods and droughts in risk management. *Nature*,
537 608(7921), 80–86. <https://doi.org/10.1038/s41586-022-04917-5>
- 538 Kumar, R., & Mishra, V. (2020). Increase in Population Exposure Due to Dry and Wet Extremes
539 in India Under a Warming Climate. *Earth's Future*, 8(12), e2020EF001731.
540 <https://doi.org/10.1029/2020EF001731>
- 541 Levy, A. A. L., Ingram, W., Jenkinson, M., Huntingford, C., Hugo Lambert, F., & Allen, M.
542 (2013). Can correcting feature location in simulated mean climate improve agreement on
543 projected changes? *Geophysical Research Letters*, 40(2), 354–358.
544 <https://doi.org/10.1002/2012GL053964>
- 545 Lin, N. (2019). Tropical cyclones and heatwaves. *Nature Climate Change*, 9(8), 579–580.
546 <https://doi.org/10.1038/s41558-019-0537-2>
- 547 Lu, E. (2009). Determining the start, duration, and strength of flood and drought with daily
548 precipitation: Rationale. *Geophysical Research Letters*, 36(12).
549 <https://doi.org/10.1029/2009GL038817>
- 550 McMichael, A. J. (2015). Extreme weather events and infectious disease outbreaks. *Virulence*,
551 6(6), 543–547. <https://doi.org/10.4161/21505594.2014.975022>
- 552 Nangombe, S., Zhou, T., Zhang, W., Wu, B., Hu, S., Zou, L., & Li, D. (2018). Record-breaking
553 climate extremes in Africa under stabilized 1.5 °C and 2 °C global warming scenarios. *Nature*
554 *Climate Change*, 8(5), 375–380. <https://doi.org/10.1038/s41558-018-0145-6>

- 555 NWS (National Weather Service). (2011). Heat Index Calculation. Retrieved March 26, 2023,
556 from <https://www.wpc.ncep.noaa.gov/html/heatindex.shtml>
- 557 O'Neill, B. C., Tebaldi, C., van Vuuren, D. P., Eyring, V., Friedlingstein, P., Hurtt, G., et al.
558 (2016). The Scenario Model Intercomparison Project (ScenarioMIP) for CMIP6. *Geoscientific
559 Model Development*, 9(9), 3461–3482. <https://doi.org/10.5194/gmd-9-3461-2016>
- 560 Park, C.-E., & Jeong, S. (2022). Population Exposure Projections to Intensified Summer Heat.
561 *Earth's Future*, 10(2), e2021EF002602. <https://doi.org/10.1029/2021EF002602>
- 562 Swain, D. L., Wing, O. E. J., Bates, P. D., Done, J. M., Johnson, K. A., & Cameron, D. R.
563 (2020). Increased Flood Exposure Due to Climate Change and Population Growth in the United
564 States. *Earth's Future*, 8(11), e2020EF001778. <https://doi.org/10.1029/2020EF001778>
- 565 Thornthwaite, C. W. (1948). An Approach toward a Rational Classification of Climate.
566 *Geographical Review*, 38(1), 55–94. <https://doi.org/10.2307/210739>
- 567 Thrasher, B., Wang, W., Michaelis, A., Melton, F., Lee, T., & Nemani, R. (2022). NASA Global
568 Daily Downscaled Projections, CMIP6. *Scientific Data*, 9(1), 262.
569 <https://doi.org/10.1038/s41597-022-01393-4>
- 570 Tuholske, C., Caylor, K., Funk, C., Verdin, A., Sweeney, S., Grace, K., et al. (2021). Global
571 urban population exposure to extreme heat. *Proceedings of the National Academy of Sciences*,
572 118(41), e2024792118. <https://doi.org/10.1073/pnas.2024792118>
- 573 Vanos, J. K., Baldwin, J. W., Jay, O., & Ebi, K. L. (2020). Simplicity lacks robustness when
574 projecting heat-health outcomes in a changing climate. *Nature Communications*, 11(1), 6079.
575 <https://doi.org/10.1038/s41467-020-19994-1>
- 576 Vicente-Serrano, S. M., Beguería, S., & López-Moreno, J. I. (2010). A multiscalar drought index
577 sensitive to global warming: the standardized precipitation evapotranspiration index. *Journal of
578 Climate*, 23(7), 1696–1718.
- 579 Wang, J., Chen, Y., Tett, S. F. B., Yan, Z., Zhai, P., Feng, J., & Xia, J. (2020).
580 Anthropogenically-driven increases in the risks of summertime compound hot extremes. *Nature
581 Communications*, 11(1), 528. <https://doi.org/10.1038/s41467-019-14233-8>
- 582 Watts, N., Amann, M., Arnell, N., Ayeb-Karlsson, S., Beagley, J., Belesova, K., et al. (2021).
583 The 2020 report of The Lancet Countdown on health and climate change: responding to
584 converging crises. *The Lancet*, 397(10269), 129–170. [https://doi.org/10.1016/S0140-6736\(20\)32290-X](https://doi.org/10.1016/S0140-
585 6736(20)32290-X)
- 586 Weber, T., Bowyer, P., Rechid, D., Pfeifer, S., Raffaele, F., Remedio, A. R., et al. (2020).
587 Analysis of Compound Climate Extremes and Exposed Population in Africa Under Two
588 Different Emission Scenarios. *Earth's Future*, 8(9), e2019EF001473.
589 <https://doi.org/10.1029/2019EF001473>
- 590 Yin, J., Gentine, P., Slater, L., Gu, L., Pokhrel, Y., Hanasaki, N., et al. (2023). Future socio-
591 ecosystem productivity threatened by compound drought–heatwave events. *Nature
592 Sustainability*, 1–14. <https://doi.org/10.1038/s41893-022-01024-1>
- 593 Yule, E. L., Hegerl, G., Schurer, A., & Hawkins, E. (2023). Using early extremes to place the
594 2022 UK heat waves into historical context. *Atmospheric Science Letters*, e1159.

- 595 Zhang, G., Wang, H., Gan, T. Y., Zhang, S., Shi, L., Zhao, J., et al. (2022). Climate Change
596 Determines Future Population Exposure to Summertime Compound Dry and Hot Events. *Earth's Future*,
597 10(11), e2022EF003015. <https://doi.org/10.1029/2022EF003015>
- 598 Zhang, Q., She, D., Zhang, L., Wang, G., Chen, J., & Hao, Z. (2022). High Sensitivity of
599 Compound Drought and Heatwave Events to Global Warming in the Future. *Earth's Future*,
600 10(11), e2022EF002833. <https://doi.org/10.1029/2022EF002833>
- 601 Zhang, W., & Zhou, T. (2020). Increasing impacts from extreme precipitation on population over
602 China with global warming. *Science Bulletin*, 65(3), 243–252.
603 <https://doi.org/10.1016/j.scib.2019.12.002>
- 604 Zhao, J.-T., Su, B.-D., mondal, S. K., Wang, Y.-J., Tao, H., & Jiang, T. (2021). Population
605 exposure to precipitation extremes in the Indus River Basin at 1.5 °C, 2.0 °C and 3.0 °C warming
606 levels. *Advances in Climate Change Research*, 12(2), 199–209.
607 <https://doi.org/10.1016/j.accre.2021.03.005>
- 608 Zscheischler, J., Westra, S., van den Hurk, B. J. J. M., Seneviratne, S. I., Ward, P. J., Pitman, A.,
609 et al. (2018). Future climate risk from compound events. *Nature Climate Change*, 8(6), 469–477.
610 <https://doi.org/10.1038/s41558-018-0156-3>
- 611